Acta Biomaterialia 8 (2012) 843–851

Contents lists available at SciVerse ScienceDirect

Acta Biomaterialia

journal homepage: www.elsevier.com/locate/actabiomat

Intrinsic magnetism and hyperthermia in bioactive Fe-doped hydroxyapatite

Anna Tampieri [a,*], Teresa D'Alessandro [a], Monica Sandri [a], Simone Sprio [a], Elena Landi [a], Luca Bertinetti [b], Silvia Panseri [c], Giancarlo Pepponi [d], Joerg Goettlicher [e], Manuel Bañobre-López [f], Jose Rivas [g]

[a] Institute of Science and Technology for Ceramics—National Research Council, Faenza (RA) 48018, Italy
[b] Department of IPM Chemistry and NIS Centre of Excellence, University of Turin, Torino 10125, Italy
[c] Laboratory of Biomechanics and Technology Innovation, Rizzoli Orthopaedic Institute, Bologna, Italy
[d] Center for Materials and Microsystems, Fondazione Bruno Kessler, via Sommarive 18, 38123 Povo, Trento, Italy
[e] Karlsruhe Institute of Technology, Institute for Synchrotron Radiation, D-76344 Eggenstein-Leopoldshafen, Germany
[f] Physical Chemistry Department, University of Santiago de Compostela, E-15782 Santiago de Compostela, Spain
[g] Applied Physics Departments, University of Santiago de Compostela, E-15782 Santiago de Compostela, Spain

ARTICLE INFO

Article history:
Received 22 June 2011
Received in revised form 20 September 2011
Accepted 26 September 2011
Available online 29 September 2011

Keywords:
Hydroxyapatite
Bone regeneration
Magnetic properties
Superparamagnetism
Hyperthermia

ABSTRACT

The use of magnetic activation has been proposed to answer the growing need for assisted bone and vascular remodeling during template/scaffold regeneration. With this in mind, a synthesis procedure was developed to prepare bioactive (Fe^{2+}/Fe^{3+})-doped hydroxyapatite (Fe-HA), endowed with superparamagnetic-like properties. This new class of magnetic hydroxyapatites can be potentially employed to develop new magnetic ceramic scaffolds with enhanced regenerative properties for bone surgery; in addition, magnetic Fe-HA can find application in anticancer therapies, to replace the widely used magnetic iron oxide nanoparticles, whose long-term cytotoxicity was recently found to reach harmful levels. An extensive physicochemical, microstructural and magnetic characterization was performed on the obtained Fe-HA powders, and demonstrated that the simultaneous addition of Fe^{2+} and Fe^{3+} ions during apatite nucleation under controlled synthesis conditions induces intrinsic magnetization in the final product, minimizing the formation of magnetite as secondary phase. This result potentially opens new perspectives for biodevices aimed at bone regeneration and for anti-cancer therapies based on hyperthermia.

1. Introduction

In recent years magnetic nanoparticles (MNPs) have received significant attention owing to their potential biomedical applications [1–3]. Indeed magnetic particles have been progressively incorporated as support materials for enzyme immobilization, and have been used as drug-delivery agents, contrast agents for magnetic resonance imaging (MRI) as well as heat mediators for hyperthermia-based anti-cancer treatments and many other exciting biotechnological applications [4–7]. Nanoparticles are amorphous semicrystalline structures with at least one dimension ranging between 10 and 100 nm. A number of their characteristics, e.g. size uniformity, surface area, adsorption kinetics, superparamagnetism and magnetic moment, can be finely tuned during the production process for specific purposes [8]. Among the most popular MNPs used in medicine [9] and biotechnology [10,11] are iron oxide-based phases (maghemite or magnetite) whose long-term effects in the human body are not yet fully assessed [12,13]. Such materials are classified as "superparamagnetic", indicating their ability to become magnetized upon exposure to a magnetic field without showing permanent magnetization (remanence) once the field is turned off. This ability is used in nanomedicine as an efficient tool to move nanoparticles into the body towards target organs. One of the most important criteria in using MNPs is the absence of any toxicity: to this end, over the last decade the surface of MNPs has been modified through the creation of biocompatible layers made of organic polymers, inorganic phases or metals deposited on the existing surface [14]. Due to the importance of having no- toxic MNPs for the above-mentioned applications, the present work is focused on the development of an innovative biocompatible and bioresorbable superparamagnetic-like phase by doping hydroxyapatite (HA) with Fe ions, avoiding the presence of poorly tolerated magnetic secondary phases. This new magnetic apatite could represent, by virtue of its bioactivity, a conceptually new type of scaffold for hard tissue regeneration. At present the use of magnetic stimulation or guidance in the field of regenerative medicine is coming up as one of the most attractive concepts [15,16]. The use of magnetic fields influencing and addressing cell behavior has been already described [17,18] and more recently it became the basic concept to design new

* Corresponding author. Tel.: +39 0546 699753; fax: +39 0546 46381.
E-mail address: anna.tampieri@istec.cnr.it (A. Tampieri).

1742-7061/$ - see front matter © 2011 Acta Materialia Inc. Published by Elsevier Ltd. All rights reserved.
doi:10.1016/j.actbio.2011.09.032

magnetizable scaffolds able to be activated by an external magnetic field [19,20]. Besides a direct stimulating influence on cells, the in vivo behavior of a magnetizable scaffold can be finely tuned by injecting MNPs as shuttles for active biomolecules (VEGF, BMP, etc.), driving signals towards the scaffolds [21,22] that stimulate bone regeneration and vascular remodeling.

This new magnetic apatite could also be a valid bioactive, bioresorbable and non-toxic substitute for magnetite in magnetic-based therapies such as hyperthermia. Hyperthermia, which in this context refers to raising the local temperature for limited periods of time, is an effective treatment for different types of cancer. Tumoral cells can be killed by exposing MNPs, deliberately placed in proximity of the tumoral tissues, to an external magnetic field.

The use of Fe-HA particles in place of magnetite, which has completely dominated the MNP market but has also given rise to concerns about its long-term toxicity, can significantly extend the use of all kinds of magnetic-based therapies.

Although Fe is a vital element in the human body, its concentration within hard tissue is low and its presence into the body scarcely affects bone remodeling [23]. On the other hand, the biocompatibility and bioactivity of HA is already well established [24–27] and in fact more than 60% of the currently available bone graft substitutes involve calcium phosphate-based materials [28]. In this view the design of a new Fe-HA phase endowed with superparamagnetic ability is very promising for application either as active scaffold for bone and osteochondral regeneration or as nontoxic biodegradable magnetic nanocarriers.

The inclusion of Fe ions in the apatite lattice has been already studied in a previous work: Ming Jiang et al. [29] studied only the local geometry and the distribution of Fe^{2+} and Fe^{3+} in the HA lattice, neglecting the investigation of any intrinsic magnetic properties. The authors found that Fe^{2+} and Fe^{3+} preferentially occupy specific crystal sites in the HA lattice, i.e. Fe^{3+} in the Ca(1) and Fe^{2+} in the Ca(2) position, which correspond to 4*f* and 6*h* sites having respectively No. 4 and No.6 calcium ions.

Other authors have reported a synthesis procedure for magnetic HA that involves introducing only Fe^{2+} ions during the neutralization process [30–33]. In particular, Wu et al. [33] measured the magnetic properties of such synthesized powder but did not discriminate between the actual formation of a new Fe-HA and magnetite as secondary phase, which indeed represented the main contributor to the magnetization signal.

The present paper takes inspiration from the fact that, in principle, it is possible to introduce both Fe species into the HA lattice at different Ca sites with a specific coordination [29] in order to generate two different sublattices whose interaction could induce superparamagnetic behavior. With this purpose, we developed and optimized a synthetic procedure to obtain a magnetic (Fe^{2+},Fe^{3+})-lattice substituted HA, minimizing the formation of magnetite as secondary phase.

2. Experimental

2.1. Synthesis methods

To prepare Fe-HA powder, a phosphoric acid (Aldrich, 85 wt.% pure, 44.40 g in 300 ml H_2O) solution was added dropwise into a basic suspension of calcium hydroxide $Ca(OH)_2$, (Aldrich, 95 wt.% pure, 50 g in 400 ml H_2O) containing Fe ions, over a period of 2 h, under constant heating and stirring. The total amounts of Fe ions with respect to Ca ions were adjusted so as to obtain: Fe/Ca = 20 - mol.%. To study the relationship between the synthesis parameters and physicochemical properties of the powders, the process was carried out in the temperature range 25–60 °C and pH decreased from 12 to 5 during neutralization. The reaction products were kept in suspension by constant stirring and heating for 1 h, and then left to age for 24 h at room temperature without further stirring. The precipitate was separated from mother liquor by centrifugation, then washed with distilled water and centrifuged three times; finally it was freeze-dried and sieved at 150 μm. This synthesis procedure was differentiated in three different methods on the basis of the Fe source used to obtain Fe^{2+}/Fe^{3+} co-doped HA nanopowders.

2.1.1. Method 1: reductive process

$FeCl_3{\cdot}6H_2O$ (Aldrich, 97 wt.% pure, 35.72 g in 150 ml H_2O) was used as a source of Fe^{3+} ions to substitute Ca^{2+} during the nucleation of HA, carried out at 40 °C. A reductive process was subsequently applied on the freeze-dried and sieved material to convert some of the Fe^{3+} into Fe^{2+} ions and to maintain both

Table 1
Characteristics of powders prepared by method 1 + reductive process.

Sample code	Fe_{tot} wt.%[a]	Fe-HA						M ($Am^2 Kg^{-1}$)
		Fe^{3+} w.t%	Fe^{2+} wt.%[b]	Fe^{3+}/Fe^{2+} wt.	Fe/Ca% mol.[a]	Ca/P mol.[a]	(Fe + Ca)/P mol.[a]	
A	10.42	6.28	4.14	1.52	27.92	1.31	1.68	0.00
B	10.42	3.10	7.32	0.42	27.92	1.31	1.68	0.00
C	10.42	0.83	9.59	0.09	27.92	1.31	1.68	0.00

[a] Mean values calculated by ICP analysis have a relative standard deviation (RDS) of 2%.
[b] Mean values calculated by UV analysis have a relative standard deviation (RDS) of 2%.

Table 2
Characteristics of powders prepared by method 2.

Sample code	Fe_{tot} wt.%[a]	Magnetite			Fe-HA						M ($Am^2 Kg^{-1}$)
		vol.%	wt.%	Fe_{tot} wt.%	Fe^{3+} wt.%	Fe^{2+} wt.%[b]	Fe^{3+}/Fe^{2+} wt.	Fe/Ca% mol.[a]	Ca/P mol.[a]	(Fe + Ca)/P mol.[a]	
D T = 25 °C	8.71	0.0	0.0	0.0	7.41	1.30	5.70	22.78	1.41	1.73	0.00
E T = 40 °C	8.80	3.0	4.8 ± 0.2	3.5	4.26	1.04	4.10	13.51	1.51	1.72	0.34 ± 0.01
F T = 60 °C	9.09	5.5	8.7 ± 0.2	6.3	0.32	2.47	0.13	6.97	1.49	1.61	0.56 ± 0.01

[a] Mean values calculated by ICP analysis have a relative standard deviation (RDS) of 2%.
[b] Mean values calculated by UV analysis have a relative standard deviation (RDS) of 2%.

Table 3
Characteristics of powders prepared by method 3.

Sample code	Fe_{tot} wt.%[a]	Magnetite			Fe-HA						M ($Am^2 Kg^{-1}$)
		vol.%	wt.%	Fe_{tot} wt.%	Fe^{3+} wt.%	Fe^{2+} wt.%[b]	Fe^{3+}/Fe^{2+} wt.	Fe/Ca% mol.[a]	Ca/P mol.[a]	(Fe + Ca)/P mol.[a]	
G T = 25 °C	9.26	0.0	0.0	0.0	8.39	0.87	9.64	26.63	1.31	1.66	0.15 ± 0.01
H T = 40 °C	9.93	1.6	2.6 ± 0.2	1.9	6.03	2.00	3.01	19.89	1.41	1.68	0.95 ± 0.01
K T = 60 °C	9.61	2.0	3.2 ± 0.2	2.3	5.26	2.05	2.56	17.99	1.44	1.69	1.20 ± 0.01

[a] Mean values calculated by ICP analysis have a relative standard deviation (RDS) of 2%.
[b] Mean values calculated by UV analysis have a relative standard deviation (RDS) of 2%.

species in the HA lattice. The process was performed at 300 °C in a closed autoclave (Parr, Alloy C276) for 1 h under continuous stirring. A gas mixture Ar/H_2 (96:4) was used as a reductive atmosphere at different pressures: 0.1 MPa (sample A), 1.9 MPa (sample B) and 2.8 MPa (sample C). The characteristics of the obtained samples are reported in Table 1.

2.1.2. Method 2: oxidative process

$FeCl_2{\cdot}4H_2O$ (Aldrich, ⩾99 wt.% pure, 25.48 g in 150 ml H_2O) was used as a source of Fe^{2+} ions and (Fe^{2+},Fe^{3+})-HA was synthesized, exploiting the spontaneous oxidation of Fe^{2+} ions, due to the reaction environment. Different synthesis temperatures were used: 25, 40 and 60 °C; the respective products were coded D, E and F (see Table 2).

2.1.3. Method 3: simultaneous addition

$FeCl_2{\cdot}4H_2O$ (Aldrich, ⩾99 wt.% pure, 12.74 g in 75 ml H_2O) and $FeCl_3{\cdot}6H_2O$ (Aldrich, 97 wt.% pure, 17.86 g in 75 ml H_2O) were added together as sources of Fe^{2+} and Fe^{3+} ions during the neutralization process. Different synthesis temperatures were investigated (25, 40 and 60 °C) and the synthesis products identified as samples G, H and K, respectively (Table 3).

2.2. Chemical, structural and magnetic characterizations

The phase composition was determined by X-ray powder diffraction (XRD), performed by a D8 Advance Diffractometer (Bruker, Karlsruhe, Germany) using CuK_α radiation at 40 kV and 40 mA. XRD spectra were recorded in the 2θ range 10–60° or 15–120°, with a step size of 0.02 and a counting time of 1 s (corresponding to 185 s using a conventional detector). Quantitative evaluation of phase compositions and cell parameters was performed by full-profile Rietveld analysis of the XRD spectrum (TOPAS v. 4.2, Bruker AXS, Karlsruhe, Germany). Computer simulation of XRD patterns of Fe-HA powders based on structural models was carried out by the aid of the software Powder cell 2.4 (W. Krause and G. Nolze, 2000).

Quantitative inductively coupled plasma–atomic emission spectrometry (ICP-OES) analysis, using an (ICP-OES: Liberty 200, Varian, Clayton South, Australia), was applied to determine the overall content of Ca, P and Fe. Samples were previously prepared as follows: 20 mg of powder were dissolved in 2 ml of HNO_3 (Aldrich, 65 wt.% pure) and the solution volume was increased up to 100 ml with deionized water. The obtained values were expressed in terms of (Fe + Ca)/P mol, Ca/P mol and Fe/Ca molar%.

The amount of Fe^{2+} was measured by a colorimetric method [34] based on the use of orthophenantroline (Merck 1,10-phenantroline, ⩾99% pure): ferrous ions in the presence of orthophenantroline form a stable red-orange complex $[(C_{12}H_8N_2)_3Fe]^{2+}$ in the pH range 4–5; this complex is detectable at 510 nm by UV–Visible spectrophotometry (Lambda 35 UV/VIS Spectrometer; Perkin Elmer Instrument, USA). 20 mg of powder were dissolved in 0.8 ml of H_2SO_4 (Aldrich, 96 wt.% pure) after having verified that sulfuric acid did not affect the concentration of the Fe^{2+}-complexed compound, at least in the time required to make the analysis. 10 ml of sodium citrate (0.5 M) were added to the solution containing sulfuric acid to set the pH around 4-5, then orthophenantroline (0.1 M) was added to the solution to set the molar ratio Fe^{2+}/orthophenantroline at 1/3. The volume of the final solution was increased up to 50 ml using deionized water.

The amount of Fe^{3+} was calculated by the difference between the total amount of Fe (determined by ICP) and the total amount of Fe^{2+} (determined by UV–VIS). The concentration of Fe^{2+} and Fe^{3+} associated to HA was derived by subtracting the contribution of Fe^{2+} and Fe^{3+} forming magnetite (detected by XRD and quantified by Rietveld refinement) from the total amount of Fe^{2+} and Fe^{3+} determined by ICP and UV analysis.

To gain information about the local chemical environment of Fe, X-ray absorption spectroscopy (XAS) at the Fe *K*-edge has been performed at the SUL-X beamline of the synchrotron radiation source ANKA (Karlsruhe Institute of Technology; Karlsruhe, Germany). SUL-X is a beamline with a wiggler as radiation source. A Si (1 1 1) crystal pair with a fixed beam exit was used as a monochromator. Higher harmonics have been suppressed by a silicon mirror behind the double-crystal monochromator. The beam was focused on the sample position by Kirkpatrick–Baez mirrors to about 100 × 100 μm. Fe *K*-edge XAS data were acquired in transmission (with ionization chambers as detectors) and fluorescence modes. The Fe concentration of the Fe-HA samples was sufficient to use the transmission data for evaluation. Energy was calibrated using a 3 μm thick Fe foil—mounted between the second and third ionization chambers—to the first inflection point of the Fe *K*-edge at 7112 eV. A typical scan ranges from 150 to 50 eV with a 5 eV energy step width and from 50 to 20 eV with a 2 eV step width prior to the edge. In the edge region between 7092 and 7142 eV the step width has been decreased to 0.3 eV, and above the edge, in the EXAFS region, up to k = 16, a k step width of 0.5 has been chosen. The measurement time per scan was 1 s, increasing with $k^{0.5}$ above the edge. Two scans have been performed on two different sample positions for Fe-HA-F and at one sample position for Fe-HA-H. Spectra were pre-edge and post-edge background corrected, and normalized to an edge jump of 1 using the Athena programme of the IFFEFIT package [35]. Reference spectra of magnetite (Fe_3O_4) and maghemite (γ-Fe_2O_3) have been taken from the SUL-X reference database and these were obtained with similar parameters.

The analysis of powder morphology was carried out by scanning electron microscopy (SEM; Stereoscan 360, Leica, Cambridge, UK). High-resolution transmission electron microscopy (HRTEM) analyses was performed by a JEOL JEM 3010-UHR, operating at 300 kV. As apatite samples might evolve under the electron beam, potentially leading to further crystallization and/or to a loss of constitutive water [36], observations were carried out under feeble illumination conditions (significantly lower than that indicated in the literature) to avoid any modifications of the materials during the analysis.

Magnetization (M) of Fe-HA powders at low field was measured at 34×10^{-4} N A^{-1} m^{-1} via a YSZ 01C/02C Susceptometer (Sartorius Mechatronics, Italy). Magnetic measurements were also performed at higher field in a superconducting quantum interference device (SQUID) magnetometer from Quantum Design (San Diego, CA, USA), capable of operating from 1.8 to 350 K under a maximum applied magnetic field of H = 5 N A^{-1} m^{-1}. In this case, about 20 mg of powder were measured from 5 to 300 K at an applied magnetic field of H = 0.01 N A^{-1} m^{-1} in order to obtain the magnetization vs. temperature (M vs. T) curves, while the magnetization vs. magnetic field (M vs. H) curves were measured in a magnetic field cycle from 2 to −2 N A^{-1} m^{-1} at T = 300 K. Measurements of magnetically induced heating were performed by placing each sample in the center of a coil of a homemade device generating an alternating magnetic field of 0.03 N A^{-1} m^{-1} at a frequency v = 293 kHz.

2.3. In vitro biocompatibility tests

Preliminary biocompatibility tests were performed by evaluating osteoblast adhesion, spreading and cell release of lactate dehydrogenase (LDH). Trabecular bone collected from adult rabbit was minced, washed and transferred to tissue culture flasks containing Dulbecco modified Eagle's medium (DMEM)/10% fetal bovine serum (FBS) and penicillin/streptomycin (100/100 U). Osteoblast outgrowth occurred after 7–10 days. Cells were expanded to passage 3 for subsequent experiments. Cells were then seeded on tablets (obtained by cold pressing Fe-HA and HA powders) (1×10^5 ml^{-1}). 24 h after seeding, phalloidin staining was performed to assess cell adhesion. After permeabilization with 0.5% Triton X-100 for 15 min, FITC-conjugated phalloidin solution (1:500 in PBS) was added for 30 min at 37 °C. Samples were washed and examined by an inverted fluorescence microscope (Nikon Ti-E, Nikon Corporation, Tokyo, Japan). Extracts for indirect tests were obtained from materials under standardized conditions (ISO 10993-5). The pure extracts, were added to cells, seeded in 24 multiwell plates 24 h before (2×10^4 ml^{-1}). Cells were incubated for the following 24 h. Cells seeded without any extract are considered as a blank group. Cells incubated with HA extract and 0.05% phenol are considered as a negative control and positive control, respectively. At the end of the experiment, supernatant from all wells was collected for LDH assay (enzymatic kinetic UV method, Futura System). The experiment was repeated six times and the results presented are the mean of the values. The data collected were statistically analyzed by one-way ANOVA ($P < 0.05$).

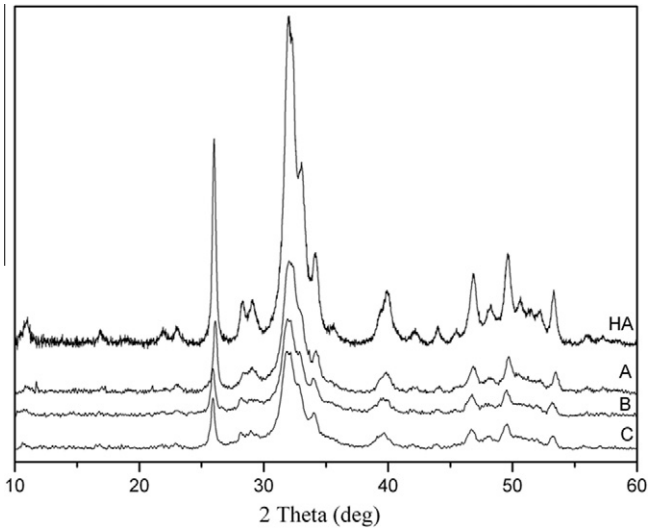

Fig. 1. XRD profiles of the HA synthesized at T = 40 °C and samples obtained by a reductive process at different pressures applied to a Fe-HA powder synthesized by method 1 at T = 40 °C.

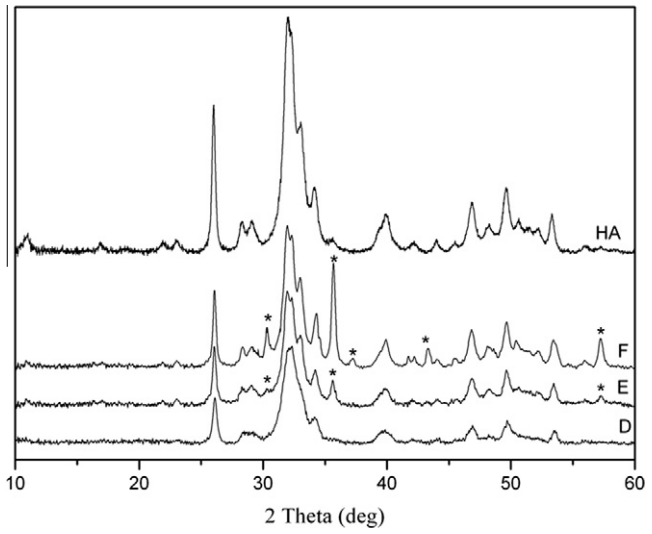

Fig. 2. XRD profiles of the HA synthesized at T = 40 °C and Fe-HA synthesized by method 2 at different temperatures (D = 25 °C; E = 40 °C; F = 60 °C). The peaks identified by ∗ correspond to magnetite.

3. Results and discussion

Fe-HA powders obtained by the three synthesis methods are characterized by primary particles in the range 5–20 nm agglomerated in larger grains of about 5–10 μm as revealed by SEM analysis.

ICP analysis confirms the presence of Fe in the powders at a level of 90% with respect to the one nominally introduced as reagent. For all the prepared Fe-HA samples, the molar ratio (Fe + Ca)/P ranges between 1.61 and 1.73 (Tables 1–3), while Ca/P ratio is lower than the theoretical one: 1.31 < Ca/P < 1.51 (Tables 1–3), confirming the replacement of Ca with Fe.

For all products, XRD spectra reveal a low-crystalline apatite (ICDD card no. 09-0432) with a crystallinity extent much lower than the non-substituted HA prepared at the same temperature (see Figs. 1–3), while the presence and amount of secondary phases can be related to the synthesis methods and parameters as explained below.

XRD structural analysis confirms the substitution of Fe ions into the HA lattice. Computer simulations clearly indicate that the Fe ions found in the HA lattice are not situated at cell interstitial positions but at Ca-substituting positions (with small differences between the 4*f* and 6*h* positions). In fact, the substitution of one Ca^{2+} ion by Fe^{2+} or Fe^{3+}, both in 4*f* and 6*h* positions, has little effect on the intensity of the diffracted X-ray lines. On the other hand, the introduction of one Fe^{2+} or Fe^{3+} ion into one of the possible interstitial positions (2*b*, 2*c*, 2*d*, 4*a* and 6*g*) heavily modifies the line intensities, always making the calculated pattern rather different from the observed one and significantly increasing the discrepancy factor. It can be observed that even if the Fe substitution into the HA lattice does not remarkably twist the structure, the presence of Fe and/or Fe–O species during HA nucleation hampers the crystallite organization. The average crystallite size is 14 ± 2 nm instead of the 5 ± 1 nm expected on the basis of the low degree of crystallinity. In this case the concept of "crystallinity", which describes the nuance of structures existing from the amorphous to the short-range order, subtends a complex scenario where the structural coherence length is at the nanometric scale, but coexists

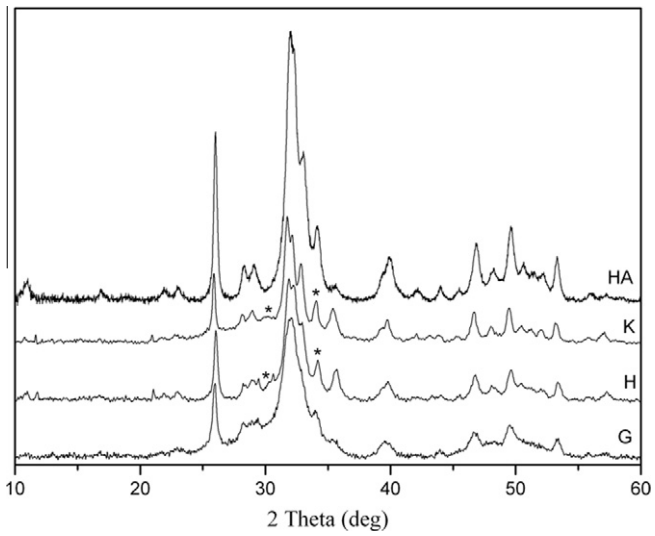

Fig. 3. XRD profiles of the HA synthesized at T = 40 °C and Fe-HA synthesized by method 3 at different temperatures (G = 25 °C; H = 40 °C; K = 60 °C). The peaks identified by ∗ correspond to magnetite.

with larger, less coherent crystallites [36]. In sample H an increase in the *a* axis from 9.4218(5) to 9.4557(1) and a decrease in *c* from 6.8813(3) to 6.8785(1) were detected by Rietveld analysis. This result is in agreement with a previous work where *c* axis diminished in Fe-substituted HA, as expected in case of substitution with ion species having a lower radius, and the *a* axis expanded, suggesting the presence of oxyhydroxyapatite [37].

The XRD analysis of the powders prepared following method 1 reveals no secondary phases apart from HA whose crystallinity increases with synthesis temperature: the degree of crystallinity is ~8% at 40 °C and ~30% at 60 °C [36]. Fe is present in HA only in its higher oxidation state and the powder does not show any magnetization signal. After application of the reductive process, no magnetite-like phase forms as detected by XRD (Fig. 1) and the magnetization signal is zero for samples A, B and C (Table 1). It can be supposed that the reduction of Fe^{3+} trapped into HA lattice, which occurs at the heterogeneous gas–solid interface, is not homogeneous throughout the whole bulk and cannot ensure a balanced distribution of Fe^{2+} and Fe^{3+} inside the structure [38].

The powders prepared following synthesis method 2 have characteristics strictly dependent on the synthesis temperature as shown in Table 2: the formation of magnetite starts at T ⩾ 40 °C as also reported in a previous work [39]. It follows that magnetite is absent in sample D and the HA crystallinity is very low (see XRD profiles in Fig. 2) [40]; in these samples no magnetization was detected. Increasing the temperature causes the kinetics of both magnetite formation and apatite crystallization to increase: XRD patterns of samples E and F (Fig. 2) show the peak of magnetite at $2\theta \approx 36°$ which strengthens when the synthesis temperature is increased. The magnetization value increases with magnetite content and for sample E and F it seems reasonable to link magnetization mainly to magnetite formation. From XRD performed in the intermediate synthesis steps, it is possible to sketch the following steps: at T ⩾ 40 °C when pH ≈ 12 only the formation of HA occurs, including Fe^{2+} into the lattice as the only available Fe species. At 11 < pH < 12 the precipitation of ferrous hydroxides occurs; the latter are recognized to be determinative in inducing magnetite formation [39]. When the pH lowers to 11 and below, the oxidation of Fe^{2+} ions starts, forming $(Fe^{3+})_2(Fe^{2+})(OH)_8$; then, at pH <10, Fe^{2+} and Fe^{3+} become free species. In this condition at T ⩾ 40 °C the formation of magnetite is favoured and at T = 60 °C (sample F) the formation of magnetite is so fast that it uptakes all Fe^{3+} ions formed following oxidation and the only Fe species found into the HA lattice is Fe^{2+} (Table 2).

The simultaneous addition of both Fe species makes both Fe^{2+} and Fe^{3+} available simultaneously during the first stage of the HA nucleation (synthesis method 3). In sample G (Table 3) magnetite is absent as expected for a synthesis temperature of 25 °C [39]; the crystallization extent of HA is very low and the lack of organization of the HA lattice reflects also the poor coordination level of the Fe ions substituting calcium; accordingly in such samples the magnetization was low (M = 0.15 A m^2 kg^{-1}).

At T = 40 °C (sample H) the formation of magnetite is minimized when compared with method 2 since both ions preferentially enter the newly formed HA (Fig. 3). In fact, HA formation starts already at pH 12: under such pH conditions both types of Fe ions are simultaneously available to enter the HA lattice occupying the favoured coordination position. At pH ⩽12 the interaction of Ca with both free Fe species hampers the formation of magnetite; similarly the presence of Fe^{3+}, at 10 < pH < 12 retards the formation of magnetite, thus stabilizing the FeOOH species as previously stated [39]. The highest effectiveness of Fe^{2+} and Fe^{3+} substitution into the HA lattice is reached in sample H where it approaches a nominal doping of 20 mol.%. The (Fe + Ca)/P ratio is 1.68 which corresponds to the theoretical Ca/P ratio for HA, and the content of magnetite is only 1.6 vol.% (Table 3). In spite of the low amount of magnetite detected in sample H, the magnetization value was high (Table 3); this can be justified only on the basis of an additional contribution due to the formation of a new magnetic phase [41]. A further increase of the synthesis temperature up to 60 °C (sample K) has detrimental results: the doping efficiency lowers and the formation of magnetite slightly increases (Table 3).

A thermal treatment at 700 °C for 1 h in Ar atmosphere has been applied to samples H and E, giving sample H(t) and E(t). The thermal stability of sample H is very low, thus resulting in the formation of Fe-containing β-TCP phases; as verified by XRD the amount of HA is lowered from 98% to 13% and the Fe ions, previously contained in HA, enter the β-TCP lattice, forming $Ca_9Fe(PO_4)_7$ and $Ca_9FeH(PO_4)_7$, as previously reported by Lazoryak et al. [42,43], while the magnetite content remains nearly unchanged. Magnetization drops from 0.95 to 0.22 A m^2 kg^{-1} suggesting that the temperature induces HA (in this case Fe-HA) degradation and destroys the magnetic domains in the apatitic lattice. Contrarily, sample E is much more stable: the degradation of HA is limited (HA lowers from 97% to 72%) and the decrease in magnetization from 0.34 to

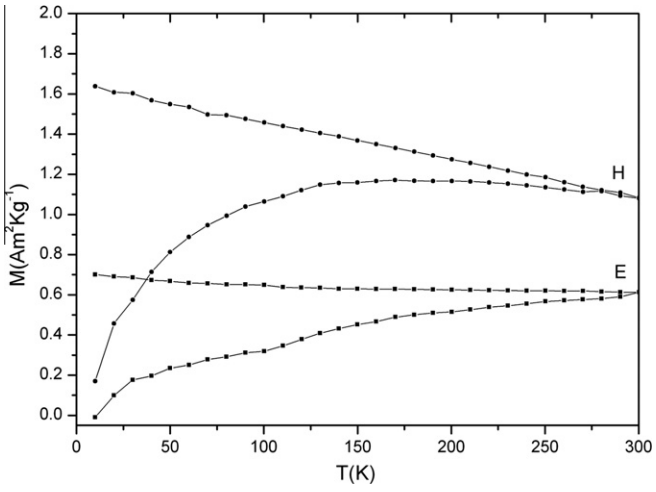

Fig. 4. Zero-field-cooled (ZFC) and field-cooled (FC) magnetization curves as a function of temperature. ZFC-FC magnetic curves for sample E (square symbol) and H (circle symbol) at an applied magnetic field of 0.01 N A^{-1} m^{-1}.

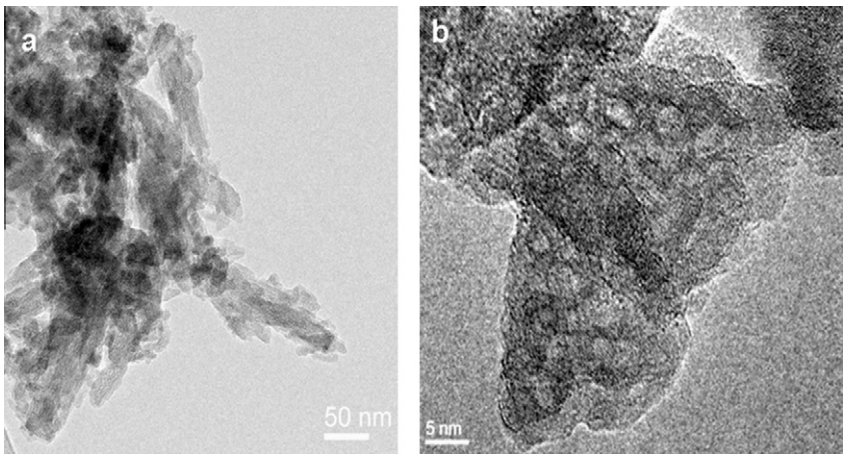

Fig. 5. TEM micrographs. (a) sample H; (b) image representing the typical Fe-HA morphology of sample H and E.

0.18 A m^2 kg^{-1} (sample E(t)) can be mainly ascribed to the decrease in magnetite content, which diminishes from 3% to 0.5%.

3.1. Relationship between microstructure and magnetic behavior of samples E and H

Detailed magnetic and microstructural characterizations were performed on samples E and H: zero-field-cooled (ZFC) and field-cooled (FC) magnetization curves as function of temperature were acquired under a high magnetic field (Fig. 4). Each sample shows behavior typical of a system of interacting magnetic particles [44]. The average blocking temperature, T_B, is found to be around 170 K for sample H, while for sample E it is beyond the measured temperature (300 K). T_B is closely related to the particle size and dipolar interparticle interactions and gets higher as the dipolar interactions increase. As a consequence of the formation of aggregates, the local concentration of nanoparticles and hence the strength of dipolar interparticle interactions increases, changing the energy barrier for magnetization relaxation and determining the collective magnetic behavior of the sample [44,45]. The significantly higher value of T_B for sample E suggests the presence of larger magnetic aggregates (ascribable to magnetite as secondary phase) in respect to sample H. This is in agreement with the XRD analysis which reports a higher concentration of magnetite in sample E vs. sample H.

In agreement with the magnetization measurements, TEM analysis of sample H shows a very low concentration of dark spots (5–10 nm in size), corresponding to inclusions of Fe-rich phases (Fig. 5). TEM investigation (Fig. 6) also confirms that the quasi-amorphous calcium phosphate matrix contains Fe uniformly distributed (as detected by energy-dispersive X-ray spectroscopy (EDS)): for both samples the micrograph in Fig. 5b shows calcium phosphate particles with needle-like morphology, rather heterogeneous in size, 5–20 nm in width and up to 50–80 nm in length.

The magnetization curves as function of the applied magnetic field for samples E and H (Fig. 7) show a superparamagnetic-like behavior of single-domain magnetic nanoparticles. Contrary to what is expected on the basis of the amount and aggregate size of magnetite, the magnetization of saturation (M_s) of sample H (4.0–4.2 A m^2 kg^{-1}) is higher than that of sample E (1.8–2.0 A m^2 kg^{-1}). The 1.6 vol.% of magnetite as secondary phase in sample H is not sufficient to justify such a magnetization value, and therefore a contribution from another magnetic phase must be involved.

As a support for this assumption, HRTEM analysis on sample H reveals that the material is made up of both amorphous and

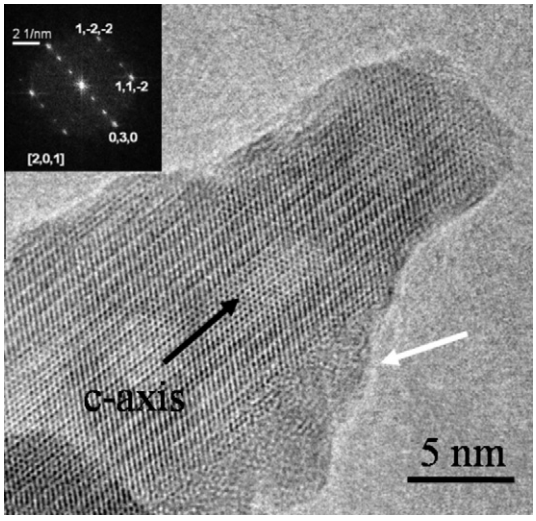

Fig. 6. High-resolution TEM micrograph of sample H observed from the [2,0,1] zone axis of HA. The black arrow indicates the orientation of the c-axis of the Fe-HA lattice retrieved from the Fourier transform of the image (inset); the white arrow points toward an amorphous region of the particle.

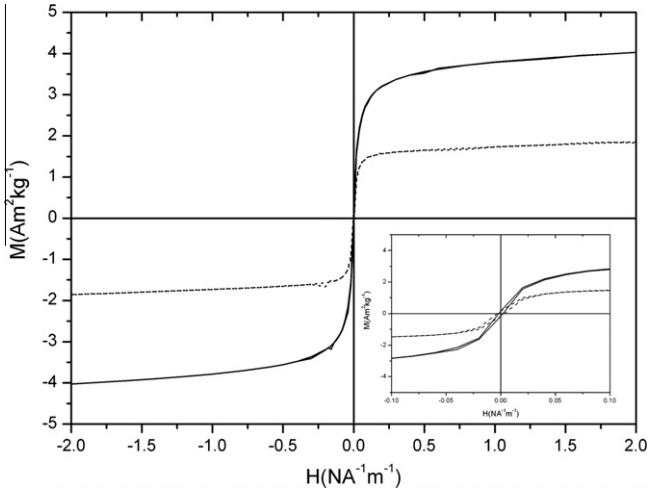

Fig. 7. Magnetic curves in function of the applied magnetic field up to 2 N A^{-1} m^{-1} for samples H (continue line) and E (dotted line) at T = 300 K.

crystalline HA domains elongated in the direction of the c-axis, which can even coexist in the same particle (Fig. 6, inset). EDS analysis (carefully choosing the apatitic matrix and avoiding the few iron oxide clusters) shows no evidence of Fe-rich phases in series of analyses on sample H. Fe appears homogeneously dispersed in the materials, probably in the form of single ions substituting Ca^{2+} in the HA lattice. The total Fe content as well as the Ca/P ratios of the calcium phosphate phase for both powders E and H has been measured by EDS (carefully choosing those regions where no iron oxide particles were detected) and the results are in good agreement with those obtained by ICP and XRD analyses reported in Tables 2 and 3.

Fig. 8a contains the XANES spectra of Fe-HA powders (i.e., samples E and H), in comparison with magnetite and maghemite, selected as reference materials. In this respect, Fe-HAs gave XANES spectra that differ from those of magnetite and maghemite, particularly concerning the different features at energies in the range 7126–7155 eV. Because of the magnetite content in the samples E and H, X-ray absorption spectra are a superposition of Fe in Fe-HA and Fe in magnetite, so that the shape of the pure Fe *K*-edge spectra of Fe-HA cannot be extracted easily. Nevertheless, the differences in shape indicate that part of the Fe does not belong to magnetite or maghemite and hence can be assigned to Fe-HA. A shift in the absorption edge (flank and whiteline) from magnetite (containing both Fe ions) to maghemite (containing only Fe^{3+}) can be observed, and can be related to different Fe^{3+}/Fe^{2+} ratios. Looking at the curves in the range between 0.5 and 1 of the edge jump, it is possible to see that the flank and the maximum position of the whiteline shift from magnetite (Fe^{3+}/Fe^{2+} ratio = 2) to sample H (Fe^{3+}/Fe^{2+} ratio = 3), sample E (Fe^{3+}/Fe^{2+} ratio = 4) and final to maghemite (Fe^{3+}/Fe^{2+} ratio = ∞).

In Fig. 8b the Fourier transform for $3.5 < k < 9$ of the EXAFS function (inset) for samples E and H, magnetite and maghemite standards are reported. Samples E and H show a higher intensity of the peak related to the first coordination shell and a shift of the bond length to higher values for both the first and the second shell when compared to maghemite and magnetite. This is in agreement with the bond length contraction from 2.43 to 2.04 Å reported by Jiang et al. [29] for substitution of Ca(1) with Fe^{3+} and also reinforces the conclusion that Fe ions are entering the HA lattice.

3.2. Hyperthermia effect

The evolution of heat vs. time of exposure to a magnetic field (hyperthermia) is reported in Fig. 9. Sample H exhibits an increase in temperature of about 40 °C in 60 s; the hyperthermia curves B and C are relative to stoichiometric HA mixed with magnetite powder (particle size ~50 nm), in the proportions 95/5 and 90/10 wt.%, respectively. Fig. 9 gives evidence of a much higher hyperthermia effect for the magnetic Fe-HA powder in comparison with the HA–magnetite mixtures, which exhibit lower increases of temperature over longer times. Since the two HA–magnetite mixtures contain higher amounts of magnetite (5 and 10 wt.%) compared to sample H (magnetite = 1.6 vol.%, i.e. ~2.6 wt.%), the intense hyperthermia herein detected cannot be explained only by the presence of magnetite and a bulk effect due to the existence of a new magnetic HA phase must be called into question. For a better understanding of its heating properties this new magnetic phase should be further investigated. The magnetic heating of superparamagnetic samples under an applied alternating magnetic field takes place fundamentally through two different physical mechanisms related to the relaxation time of the magnetic moment: Neél and Brownian relaxations. In the case of a solid sample that is not dispersed in a liquid, only the Neél relaxation should be taken into account. In this scenario, the saturation magnetization is not the only parameter that affects the heating properties, but other structural/physical parameters such as particle size and distribution, magnetic anisotropy and dipolar inter-particle magnetic interactions also play an important role and could be the cause of

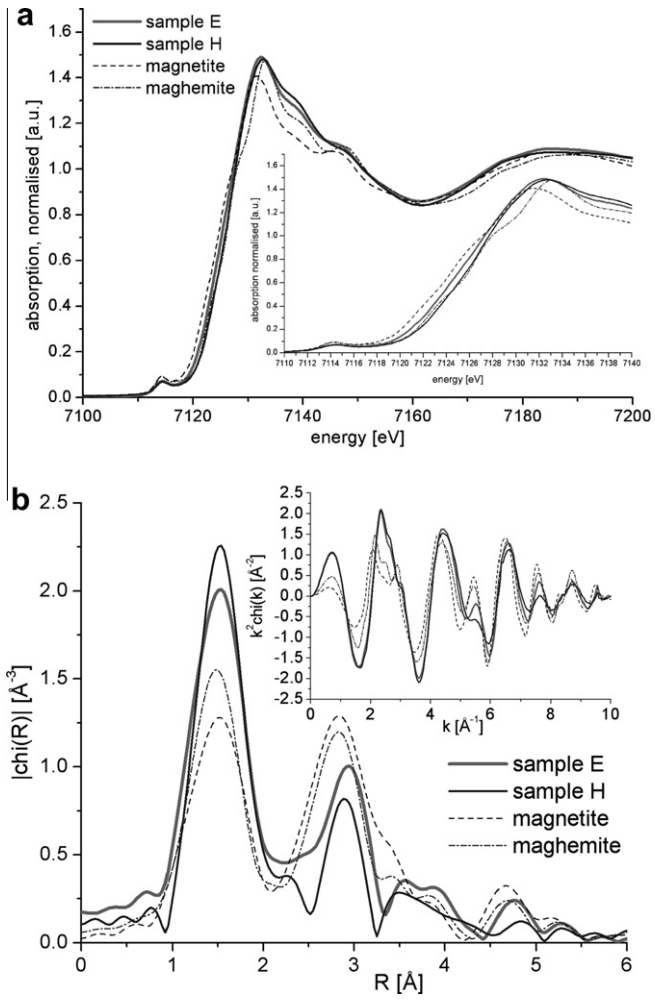

Fig. 8. Fe *K*-edge X-ray absorption near edge (XANES) spectra with edge region in the inset (a) and Fourier transform of the EXAFS function (inset), both k^2 weighted (b) for samples E and H and the magnetite and maghemite reference substances.

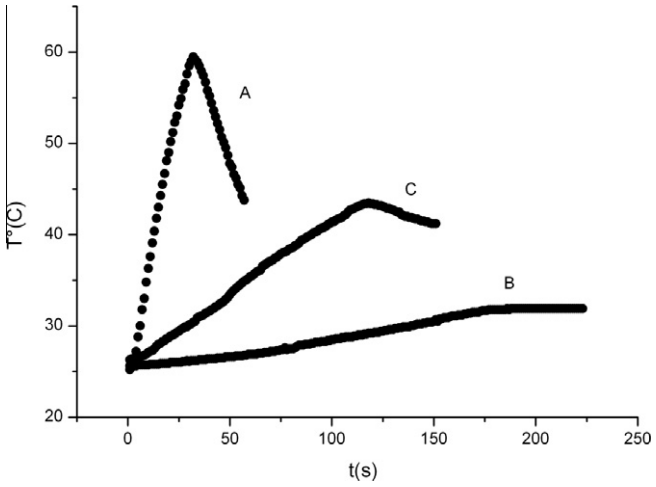

Fig. 9. Hyperthermia curves: (A) sample H, (B) mixture of HA/magnetite (95/5 wt.%) and (C) mixture of HA/magnetite 90/10 wt.%.

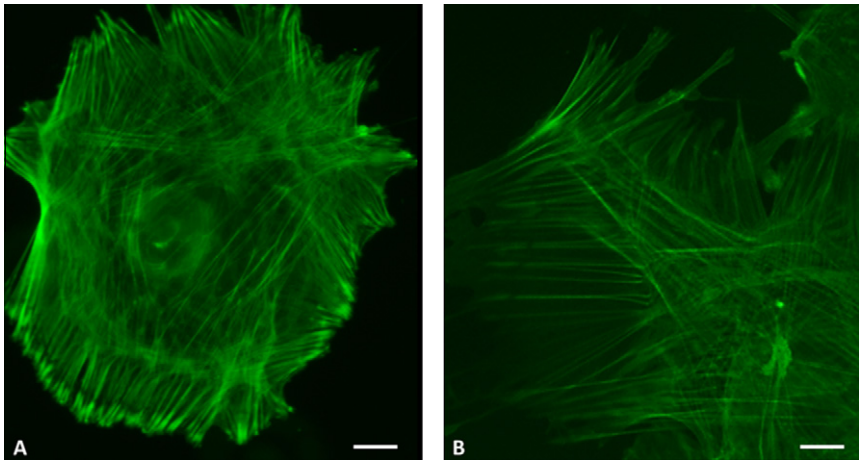

Fig. 10. Fluorescence image of attached osteoblasts on the tablet surface of sample H (A) and HA control group (B). Actin cytoskeleton of cells, stained with phalloidin, shows a good morphology. Scale bar: 10 μm.

such heating enhancement. In order to determine the nature of such hyperthermia behavior, further experiments will be addressed.

3.3. Biocompatibility tests

Compared to stoichiometric HA, the magnetic Fe-HA represents a suitable substrate, in terms of biocompatibility, for osteoblasts. The cytotoxicity evaluation performed by the LDH assay does not show any differences among groups (except between the positive control group and all the other groups, $P < 0.05$), indicating that Fe-HA, similarly to the other substrates, does not stimulate any cytotoxic response by osteoblasts after 24 h (Fe-HA: $6.81 \pm 1.32\ U\ l^{-1}$; negative group control (HA): $7.35 \pm 2.12\ U\ l^{-1}$; blank group: $7.08 \pm 1.88\ U\ l^{-1}$; positive control group: $18.75 \pm 1.89\ U\ l^{-1}$). Phalloidin stains actin filaments, thereby characterizing cytoskeletal organization and cell spreading. The images related to the analysis of phalloidin staining after 24 h seeding show a good morphology of the attached cells. Similarly to HA, the cells on the Fe-HA show a diffuse spread-like morphology (Fig. 10) [46,47].

4. Conclusions

A neutralization method has been employed to synthesize HA nanopowders in which Ca is partially substituted by Fe^{2+} and Fe^{3+}. The simultaneous addition of both Fe species under controlled synthesis conditions leads to Fe-HA with a (Fe + Ca)/P ratio very close to the theoretical one (Ca/P = 1.67), Fe^{3+}/Fe^{2+} ratio ~3 and a very small content of magnetite as secondary phase. XRD, ICP and TEM analysis confirm that both Fe^{2+} and Fe^{3+} ions enter the HA lattice. The new Fe-HA exhibits very low crystallinity and a structural coherence at the nanometer length scale together with very low thermal stability. Likewise, XANES and EXAFS spectra reveal additional contribution from the Fe *K*-edge, besides Fe in magnetite, assignable to Fe in apatite. Powder H showed the superparamagnetic-like behavior typical of single-domain magnetic nanoparticles: the signal largely exceeded the one expected for such a low content of magnetite. A relevant hyperthermia effect indicated a bulk phenomenon that even more clearly confirms the intrinsic magnetic behavior of this Fe-HA phase.

The occupation of the Ca(1) and Ca(2) crystallographic positions of the HA lattice by the two Fe species and their specific spatial distribution (which implies a specific Fe^{3+}/Fe^{2+} ratio) raised the hypothesis of two distinct interacting structural domains or sublattices, whose nature deserves further investigation, as does as the mechanism underlying the superparamagnetic effect.

The magnetic property of the new Fe-HA phase together with its biocompatibility open the door of the regenerative medicine to a conceptually new family of biomimetic scaffolds able to be biologically manipulated or activated in situ by means of an external magnetic field. Additionally, the high hyperthermia of Fe-HA offers a true advantage with respect to the present solutions in anti-cancer therapies: the benefits foreseen are not only the more intense and rapid local effect, but most of all its biocompatibility/degradability, which overcome the side effects of long-term cytotoxicity. Injected MNPs can also increase the resolution, up to the cellular scale, of diagnostic techniques such as resonance. Hence, such Fe-HA nanoparticles could be effectively used in cancer prevention, allowing further development of the resonance technique which can be improved towards the early detection of even small tumoral cell aggregates. In conclusion, regenerative medicine and the wider field of theranostics may benefit from solutions represented by these completely biocompatible and biodegradable magnetic nanocarriers.

Acknowledgements

We are very grateful to Dr. G. Celotti (ISTEC-CNR) for valuable discussion on crystallographic aspects, and we kindly thank Dr. Y. Piñeiro-Redondo (University of Santiago de Compostela) for hyperthermia measurements. We would like to acknowledge European Project MAGISTER (NMP3-LA-2008-214685) for funding our research.

Appendix A. Figures with essential color discrimination

Certain figures in this article, particularly 'Fig. 10' is difficult to interpret in black and white. The full color images can be found in the on-line version, at doi:10.1016/j.actbio.2011.09.032.

References

[1] Corchero JL, Villaverde A. Biomedical applications of distally controlled magnetic nanoparticles. Trends Biotechnol 2009;27:468–76.
[2] Gupta AK, Gupta M. Synthesis and surface engineering of iron oxide nanoparticles for biomedical applications. Biomaterials 2005;26:3995–4021.
[3] Saiyed Z, Telang S, Ramchand C. Application of magnetic techniques in the field of drug discovery and biomedicine. Biomagn Res Technol 2003;1:1–2.
[4] Ajeesh M, Francis BF, Annie J, Harikrishna Varma PR. Nano iron oxide-hydroxyapatite composite ceramics with enhanced radiopacity. J Mater Sci Mater Med 2010;21:1427–34.

[5] Ito A, Kobayashi T. Intracellular hyperthermia using magnetic nanoparticles: a novel method for hyperthermia cancer. Jap Soc Thermal Med 2008;24:113–29.
[6] Kalambur VS, Han B, Hammer BE, Shield TW, Bischof JC. In vitro characterization of movement, heating and visualization of magnetic nanoparticles for biomedical applications. Nanotechnol 2005;16:1221–33.
[7] Mornet S, Vasseur S, Grasset F, Duguet E. Magnetic nanoparticle design for medical diagnosis and therapy. J Biosci Bioeng 2005;100:1–11.
[8] Zeng H, Sun SH. Syntheses, properties and potential applications of multicomponent magnetic nanoparticles. Adv Funct Mater 2008;18:391–400.
[9] Pankhurst QA, Connolly J, Jones SK, Dobson J. Applications of magnetic nanoparticles in biomedicine. J Phys D Appl Phys 2003;36:R167–81.
[10] Ramchand CN, Priyadarshini P, Kopcansky P, Metha RV. Applications of magnetic fluids in medicine and biotechnology. Indian J Pure Appl Phys 2001;39:683–9.
[11] Schwertmann U, Cornell RM. Iron oxides in the laboratory: preparation and characterisation. Weinheim: VCH; 1991 [p. 137].
[12] Lewinski N, Colvin V, Drezek R. Cytotoxicity of nanoparticles. Small 2008;4:26–49.
[13] Singh N, Jenking GJS, Asadi R, Doak SH. Potential toxicity of superparamagnetic iron oxide nanoparticles (SPION). Nano Reviews 2010;1:53–8.
[14] Berry CC, Curtis ASG. Functionalisation of magnetic nanoparticles for applications in biomedicine. J Phys D Appl Phys 2003;36:198–206.
[15] Amirfazli A. Nanomedicine: magnetic nanoparticles hit the target. Nat Nanotechnol 2007;2:467–8.
[16] Phillips MA, Gran ML, Peppas NA. Targeted nanodelivery of drugs and diagnostics. Nano Today 2010;5:143–59.
[17] Nakamae T, Adachi N, Kobayashi T, Nagata Y, Nakasa T, Tanaka N, et al. The effect of an external magnetic force on cell adhesion and proliferation of magnetically labeled mesenchymal stem cells. Sports Med Arthrosc Rehabil Ther Technol 2010;2:1–7.
[18] Hori J, Deie M, Kobayashi T, Yasunaga Y, Kawamata S, Ochi M. Articular cartilage repair using an intra-articular magnet and synovium-derived cells. J Orthop Res 2011;29:531–8.
[19] Bock N, Riminucci A, Dionigi C, Russo A, Tampieri A, Landi E, et al. A novel route in bone tissue engineering: magnetic biomimetic scaffolds. Acta Biomater 2010;6:786–96.
[20] Tampieri A, Landi E, Valentini F, Sandri M, D'Alessandro T, Dediu V, et al. A conceptually new type of bio-hybrid scaffold for bone regeneration. Nanotechnol 2011;22:015104 [8pp].
[21] Dobson J. Magnetic nanoparticles for drug delivery. Drug Develop Res 2006;67:55–60.
[22] Foy SP, Manthe RL, Foy ST, Dimitrijevic S, Krishnamurthy N, Labhasetwar V. Optical imaging and magnetic field targeting of magnetic nanoparticles in tumors. ACS Nano 2010;4:5217–24.
[23] Morrissey R, Rodriguez-Lorenzo LM, Gross KA. Influence of ferrous iron incorporation on the structure of hydroxyapatite. J Mater Sci Mater Med 2005;16:387–92.
[24] Landi E, Celotti G, Logroscino G, Tampieri A. Carbonated hydroxyapatite as bone substitute. J Eur Ceram Soc 2003;23:2931–7.
[25] Landi E, Tampieri A, Celotti G, Sprio S, Sandri M, Logroscino G. Sr-substituted hydroxyapatites for osteoporotic bone replacement. Acta Biomater 2007;3:961–9.
[26] Landi E, Tampieri A, Mattioli-Belmonte M, Celotti G, Sandri M, Gigante A, et al. Biomimetic Mg- and Mg, CO_3-substituted hydroxyapatites: synthesis characterization and in vitro behaviour. J Eur Ceram Soc 2006;26:2596–601.
[27] LeGeros RZ. Calcium phosphates in oral biology and medicine. In: Myers HM, editor. Monographs in oral science. New York: Karger; 1991. p. 82–128.
[28] Laurencin C, Khan Y, El-Amin SF. Bone graft substitutes. Expert Rev Med Devices 2006;3:49–57.
[29] Jiang M, Terra J, Rossi MA, Morales MA, Saitovitch EMB, Ellis DE. Fe^{2+}/Fe^{3+} substitution in hydroxyapatite: theory and experiment. Phys Rev B: Condens Mater Phys 2002;66:224107–15.
[30] Gross KA, Jackson R, Cashion JD, Rodriguez-Lorenzo LM. Iron substitute apatites: a resorbable biomaterial with potential magnetic properties. Eur Cells Mater 2002;3:114–7.
[31] Hou CH, Hou SM, Hsueh YS, Lin J, Wu HC, Lin FH. The in vivo performance of biomagnetic hydroxyapatite nanoparticles in cancer hyperthermia therapy. Biomaterials 2009;30:3956–60.
[32] Wu HC, Wang TW, Bohn MC, Lin FH, Spector M. Novel magnetic hydroxyapatite nanoparticles as non-viral vectors for the glial cell line-derived neurotrophic factor gene. Adv Funct Mater 2009;19:1–11.
[33] Wu HC, Wang TW, Sun JS, Wang WH, Lin FH. A novel biomagnetic nanoparticle based on hydroxyapatite. Nanotechnol 2007;18:165601–10.
[34] Potts PJ. A handbook of silicate rock analysis. Blackie: Glasgow; 1987.
[35] Ravel B, Newville M. ATHENA, ARTEMIS, HEPHAESTUS: data analysis for X-ray absorption spectroscopy using IFEFFIT. J Synchr Rad 2005;12:537–41.
[36] Celotti G, Tampieri A, Sprio S, Landi E, Bertinetti L, Martra G, et al. Crystallinity in apatites: how can a truly disordered fraction be distinguished from nanosize crystalline domains? J Mater Sci-Mater M 2006;17:1079–87.
[37] Low HR, Phonthammachai N, Maignan A, Stewart GA, Bastow TJ, Ma LL, et al. The crystal chemistry of ferric oxyhydroxyapatite. Inorg Chem 2008;47:11774–82.
[38] Koksharov YA. Magnetism of nanoparticles: effect of size, shape and interaction. In: Gubin P, editor. Magnetic Nanoparticles. Weinheim: VCH; 2009. p. 197–246.
[39] Perez OP, Umetsu Y, Sasaki H. Precipitation and densification of magnetic iron compounds from aqueous solutions at room temperature. Hydrometallurgy 1998;50:223–42.
[40] Liu C, Huang Y, Shen W, Cui J. Kinetics of hydroxyapatite precipitation at pH 10 to 11. Biomaterials 2001;22:301–6.
[41] Tampieri A, Landi E, Sandri M, Pressato D, Rivas J, Lopez MB, Marcacci M. Italian Patent No. MI2010A001420, 2010.
[42] Lazoryak BI, Morozov VA, Belik AA, Khasanov SS, Shekhtman VS. Crystal structures and characterization of $Ca_9Fe(PO_4)_7$ and $Ca_9FeH_{0.9}(PO_4)_7$. J Solid State Chem 1996;122:15–21.
[43] Lazoryak BI, Morozov VA, Belik AA, Stefanovich SY, Grebenev VV, Leonidov IA, et al. Ferroelectric phase transition in the whitlockite-type $Ca_9Fe(PO_4)_7$; crystal structure of the paraelectric phase at 923 K. Solid State Sci 2004;6:185–95.
[44] Hoppe CE, Rivadulla F, Vidal-Vidal J, Lopez-Quintela MA, Rivas J. Magnetic relaxation of gamma-Fe_2O_3 nanoparticles arrangements and electronic phase-segregated systems. J Nanosci Nanotechnol 2008;8:2883–90.
[45] Klabunde KJ, Mulukutla RS. Nanoscale materials in chemistry. In: Klabunde KJ, editor. New York: Wiley-Interscience; 2001. p. 223–61.
[46] Deligianni DD, Katsala DN, Koutsoukos PG, Missirlis FY. Effect of surface roughness of hydroxyapatite on human bone marrow cell adhesion, proliferation, differentiation and detachment strength. Biomaterials 2001;22:87–96.
[47] Oreffo RO, Driessens FC, Planell JA, Triffitt JT. Growth and differentiation of human bone marrow osteoprogenitors on novel calcium phosphate cements. Biomaterials 1998;19:1845–54.